

Flow Field Reconstructions with GANs based on Radial Basis Functions

Liwei Hu, *Student Member, IEEE*, Wenyong Wang, *Member, IEEE*, Yu Xiang, *Member, IEEE*, Jun Zhang

Abstract—Nonlinear sparse data regression and generation have been a long-term challenge, to cite the flow field reconstruction as a typical example. The huge computational cost of computational fluid dynamics (CFD) makes it much expensive for large scale CFD data producing, which is the reason why we need some cheaper ways to do this, of which the traditional reduced order models (ROMs) were promising but they couldn't generate a large number of full domain flow field data (FFD) to realize high-precision flow field reconstructions. Motivated by the problems of existing approaches and inspired by the success of the generative adversarial networks (GANs) in the field of computer vision, we prove an optimal discriminator theorem that the optimal discriminator of a GAN is a radial basis function neural network (RBFNN) while dealing with nonlinear sparse FFD regression and generation. Based on this theorem, two radial basis function- based GANs (RBF-GAN and RBFC-GAN), for regression and generation purposes, are proposed. Three different datasets are applied to verify the feasibility of our models. The results show that the performance of the RBF-GAN and the RBFC-GAN are better than that of GANs/cGANs by means of both the mean square error (MSE) and the mean square percentage error (MSPE). Besides, compared with GANs/cGANs, the stability of the RBF-GAN and the RBFC-GAN improve by 34.62% and 72.31%, respectively. Consequently, our proposed models can be used to generate full domain FFD from limited and sparse datasets, to meet the requirement of high-precision flow field reconstructions.

Index Terms—Generative adversarial network, Radial basis function neural network, Deep learning, Aerodynamic flow field reconstruction, The optimal discriminator theorem

I. INTRODUCTION

FLOW field reconstructions [1] reflect the variation of air flows in spatial or time domain, which plays a fundamental role in the field of shape optimizations, inverse designs, and simulations of flight [2], [3], [4], etc. The term reconstructions denotes both the regression and generation of full domain flow field data (FFD) from given datasets [5]. Generally, considering the computational costs or inability of existing approaches of data producing, the number of data contained in flow field datasets is limited [6]. However the range of design parameters (e.g. height, Mach number, angle of attack, Reynolds number, etc) can be large, which results in the sparse nature of flow field datasets. Besides, the mapping between design parameters and response parameters (e.g. forces and

W. Wang, professor, is with School of Computer Science and Engineering, University of Electronic Science and Technology of China, Chengdu 611731, China, e-mail:wangwy@uestc.edu.cn.

W. Wang, special-term professor, is with Macau University of Science and Technology, Macau 519020, China.

L. Hu, Y. Xiang, and J. Zhang are with University of Electronic Science and Technology of China, Chengdu 611731, China.

Manuscript received April XX, XXXX; revised August XX, XXXX.

moments, etc) is highly nonlinear. The sparse and nonlinear characteristics of flow field datasets make it difficult to reconstruct flow field precisely [7]. In the area of aerodynamics, there are two different approaches to reconstruct flow field, namely full order models (FOMs) and reduced order models (ROMs) [8].

The computational fluid dynamics (CFD), a representative of the FOMs, is a high-fidelity numerical simulation [9]. CFD-based systems are the main approach to calculate high-fidelity FFD in aerodynamics. However, most of governing equations are nonlinear partial differential equations (PDEs) and have no numerical solutions. Therefore, it is impossible to calculate the aerodynamic response values under all flow states and aerodynamic shapes [10]. In addition, the large computational costs of CFD-based systems are beyond the tolerance of researchers both in time and hardware resources.

The drawbacks of FOMs motivated the development of ROMs, which can learn the nonlinear mapping between aerodynamic design parameters and response parameters from limited training data calculated by full order CFD-based systems [11], [12]. Compared with FOMs, ROMs use different convergence strategies or models to reduce the calculation time on the premise of ensuring high accuracies. Besides, ROMs can deal with both linear and nonlinear FFD. As for linear FFD processing, the linear ROMs are considered, such as the autoregressive with exogenous input model [12]. As for nonlinear FFD processing, the nonlinear ROMs must be employed, such as Kriging model [13], [14], support vector machine [15], neural network [16], [17], and block-oriented Wiener models [18], etc. However, while dealing with nonlinear FFD, a large number of training data are needed to provided by CFD-based systems to guarantee the accuracies of ROMs. What's worse, ROMs can only output response values in given flow states, and cannot generate full domain FFD that satisfy the governing equations.

Neural networks, a part of the ROMs, have attracted much attention in aerodynamics in the past few years [19], [10]. The conventional approaches are based on full connected networks (FCNs), which output response parameters under given flow states [1], [20]. However, the flow states need to be specified by researchers in advance and can not be automatically generated by FCN-based models. Hence these studies belongs to regression rather than generation. The generative adversarial networks (GANs), as new generative models, can generate full domain flow FFD from a random noise, which becomes a feasible way to solve this problem.

A GAN consists of two adversarial sub-models: the generator G and the discriminator D. The goal of D is to train a

function $D(x)$ that can be used to distinguish the real data distribution $\mathbb{P}_r(x)$ from the generated data distribution $\mathbb{P}_g(x)$. The goal of G is to train a function $G(z)$ that can generate pseudo-data from a simple data distribution $\mathbb{P}_z(z)$. D and G are trained alternately until D can not distinguish the real data from the generated data. GANs have achieved great success in the field of image generation [21], [22], image translation [23], feature analysis [24], and machine translation [25], etc. These studies demonstrated that GANs possess the capability to capture the distribution of data contained in datasets, and further map input into output space, which brings new ideas to the field of flow field reconstructions. Recently, researchers adopted GANs to reconstruct flow fields, which have become a state-of-the-art approach [26].

The existing studies in flow field reconstructions are categorized into image-based and non-image-based flow field reconstructions. In the field of image-based flow field reconstructions, the recursive CNNs-based GAN in unsteady flow predictions [27], the recurrent neural networks (RNNs)-based GAN in the analyses of the temporal continuity [28] and the tempoGAN for high-resolution flow field image generations [29] are outstanding models. All of them use flow field images as the input to train convolutional neural networks (CNN)-based GANs, and the outputs are still images. Although, these CNN-based GANs can generate high-resolution flow field images to express the variations of air flows, the non-image-based flow field reconstructions can omit the process of converting FFD into images while maintaining high accuracies. Farimani used the original FFD as a training set and adopted cGAN to study flow field reconstructions [30]. The results showed that the MAE of generated FFD was lower than that of traditional ROMs. However, this non-image-based model is not stable enough (the error fluctuates rapidly while training).

Motivated by the problems of existing approaches and inspired by the adversarial learning mechanism of GANs, we prove an theorem that a radial basis function neural network (RBFNN) is the optimal discriminator of a GAN while dealing with nonlinear sparse data come from a continuous function. Based on this theorem, a radial basis function-based GAN (RBF-GAN) and a radial basis function cluster-based GAN (RBFC-GAN), two novel data-driven models, are proposed to implement both the regression and generation for nonlinear sparse FFD¹. Different from the GANs-based models mentioned above, the advantages of our models are a) they are both regression models and generative models, which can quickly generate full domain FFD in accordance with the variation laws in flow fields; b) they are data-based interpolation models, which do not require thorough knowledge of aerodynamics and can significantly reduce the error of generated data and improve the stability of GANs; and c) the training sets of the RBF-GAN and the RBFC-GAN are nonlinear sparse FFD, not images generated from FFD. Subsequently, three different datasets are applied to verify the validity and feasibility of the proposed models. The results show that a) the mean square error (MSE) and the mean square percentage error (MSPE) [8]

¹The source code of RBF-GAN and RBFC-GAN can be found in <https://github.com/huliwei123/RBF-GANs.git>.

of the data generated by the RBF-GAN/RBFC-GAN are lower than that of data generated by full connected neural networks-based GANs; and b) compared with already proposed cGAN, the stability of the RBF-GAN and the RBFC-GAN improves by 34.62% and 72.31%, respectively.

To summarize, the contributions of our work are:

- a) we prove an theorem that an RBFNN is the optimal discriminator of a GAN while dealing with nonlinear sparse data;
- b) based on a), we propose the RBF-GAN, both a generative and a regression model, to generate full domain FFD from limited nonlinear sparse data;
- c) based on b), we propose the RBFC-GAN to further improve the fidelity of generated nonlinear sparse full domain FFD, as well as the stability of GANs after converged.

The structure of this paper is as follows. Section II introduces the research status of RBFNNs and GANs in the field of aerodynamic response predictions and flow field reconstructions, respectively. In Section III, the optimal discriminator theorem for nonlinear sparse data generation and the mechanisms of the proposed RBF-GAN and RBFC-GAN are elaborated. In Section IV, three datasets from different scenes are applied to validate the effectiveness of the proposed models. The conclusion of our work is shown in Section V.

II. RELATED WORK

In this section, we introduce the fundamental of RBFNNs and GANs, and their applications in FFD processing.

A. RBFNNs

1) *The Fundamental of RBFNNs:* An RBFNN (Fig.1), a regression model, is a three-layer feedforward neural network, which consists of one input layer, one hidden layer and one output layer [31]. Considering the combination of RBFNNs and GANs, the number of output neurons in this figure is set to 1. Different from fully connected networks (FCNs) which use sigmoid or ReLU as the activation function, an RBFNN employ an RBF instead [32]. Generally, the most commonly used RBF is the Gaussian kernel function:

$$g_1(\mathbf{x}_i, \mathbf{v}_j, \sigma_j) = \exp\left(-\frac{\|\mathbf{x}_i - \mathbf{v}_j\|^2}{2\sigma_j^2}\right)$$

where $\|\cdot\|$ is a norm on the function space, \mathbf{x}_i denotes the i th sample in the training set, \mathbf{v}_j and σ_j denote the center and width of the j th hidden neuron, respectively. The output of an RBFNN can be written as:

$$\mathbf{y}_i = w_0 + \sum_{j=1}^q \mathbf{w}_j \cdot g_1(\mathbf{x}_i, \mathbf{v}_j, \sigma_j)$$

where q denotes the number of hidden neurons, \mathbf{w}_j denotes the weight between one hidden neuron and one output neuron, and w_0 denotes the bias of the only output neurons.

Theoretically, an RBFNN converges faster than a FCN with the same number of hidden neurons. Consider an input \mathbf{x} and

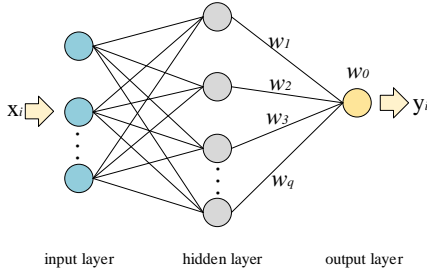


Fig. 1. The structure of an RBFNN. In particular, the center v_j of the RBF is a vector with the same dimension as the input x_i , while the width σ_j is a scalar.

two hidden neurons n_1 and n_2 with parameters $v_1 \gg v_2 = x$ and $\sigma_1 = \sigma_2 = 1$, the output of n_1 is close to 0, while the output of n_2 is 1, according to (1). Therefore, n_1 produces a gradient of 0, which leads to the result that v_1 and σ_1 remain unchanged, i.e. vanishing gradient [33]. In contrast, only v_2 and σ_2 of neuron n_2 can be updated. The approach of updating parts of the parameters is called local updating mechanism, which perfectly explains why an RBFNN converges faster than a FCN with the same structure.

2) *RBFNN-based Aerodynamic ROMs* : RBFNNs-based aerodynamic ROMs are widely used to predict aerodynamic response parameters, because of its powerful nonlinear input-output mapping ability. According to the number of kernel functions (i.e. radial basis functions), the existing studies can be categorized into two groups: single kernel RBFNNs and multi-kernel RBFNNs.

Single kernel RBFNNs are the most commonly used models in aerodynamic response predictions. In 2005, Hovcevar et al. first adopted RBFNN with Gaussian kernel function to predict the fluctuations in the passive-tracer concentration for the turbulent wake behind an airfoil [34]. The explosion of RBFNNs in aerodynamic data modeling came after 2010 [35]. Ghoreyshi applied single kernel RBFNNs to study unsteady aerodynamic modeling at low-speed flow conditions [36]. Different from Ghoreyshi, Zhang divided the whole flow field into three parts: the near-wall region, the wake region and the far-field region [37], [38]. Three single kernel RBFNNs were built to predict the eddy velocity. All these models mentioned above use the Gaussian kernel function.

Multi-kernel RBFNNs refer to those RBFNNs with multiple RBFs, which are recently studied. Kou et al. proposed a multi-kernel RBFNN, and used it to model unsteady aerodynamics [8]. Kou implemented this model by adopting the linear combination of the Gaussian kernel function and wavelet kernel function mentioned in [39]. The experimental results showed that the errors of multi-kernel neural networks is lower than that of single kernel RBFNNs in both fixed Mach number test case and variant Mach number test case.

The RBFNNs mentioned above are not applied in flow field reconstructions, because RBFNNs are interpolation models and do not have the ability to generate abundant full domain FFD. Hence, it is difficult for RBFNNs to achieve rapid and refined flow field management.

B. GANs

1) *The Fundamental of GANs*: Fig.2 illustrates the structure of a GAN, which takes a noise with specific distributions as input and outputs a variable with a value between 0 and 1. The loss functions of D and G are:

$$L_D = -\mathbb{E}_{x \sim p_r(x)}[\log D(x)] - \mathbb{E}_{z \sim p_z(z)}[\log(1 - D(G(z)))] \quad (1)$$

$$L_G = \mathbb{E}_{z \sim p_z(z)}[\log(1 - D(G(z)))] \quad (2)$$

where x denotes the real data that follow the distribution density $p_r(x)$, z denotes the input noise with the distribution density $p_z(z)$. The training goal of a GAN is to make the above two formulas reach their minimum.

Although GANs have achieved great success in many fields, they still face many problems, for example mode collapse [40], [41], convergence problem [42], vanishing gradient [43], application problems, instability [10], etc. To solve these problems, some new models, algorithms and loss functions were proposed [44]. The Wasserstein-GAN and earth-mover distance [43] essentially solved the problem of convergence, and they alleviate the problem of mode collapse. The Dual-GAN [45] and the DC-GAN [46] expands the application of GANs in the field of computer vision [47]. The conditional GAN (cGAN) [48] and the info-GAN [49] can generate desired data under specific conditions, which expand the basic application of GANs. Based on current studies, the problems of model collapse and instability are still the major issues of GANs. In this paper, our proposed models alleviate the model collapse and instability, which are discussed in Section IV.B.1) and IV.B.3), respectively.

2) *Generative Adversarial Networks-based ROMs for non-linear sparse FFD regression and generation*: In this section, we only discuss the non-image-based studies. Usually, the cGAN rather than GAN is widely used. Because most of the governing equations (e.g. Navier-Stokes equation) are partial differential equations and have no numerical solutions, which makes it infeasible to use the governing equations to evaluate errors of GANs-based models.

Farimani adopted cGANs, both regression models and generative models, to learn the transport phenomena in aerodynamics [30]. The results show that the MAE of generated data is lower than 0.01, however, the stability of cGAN-based models is not discussed. Hu et al. adopted cGANs to predict the velocity u in Burgers' equation and the coefficient of pressure C_p in Navier-Stokes equation [10]. By comparing cGANs with different structures, the stability of them is emphasized: after converged, the errors of cGANs during the training procedure fluctuates rapidly in a relatively large range, which result in that a) the designer of the models cannot decide when to stop the training process according to their experiences; and b) the models cannot generate high-fidelity full domain FFD.

As a result, existing non-image-based models are not suitable for the case of using nonlinear sparse FFD as data sets, because that the errors of generated FFD is relatively

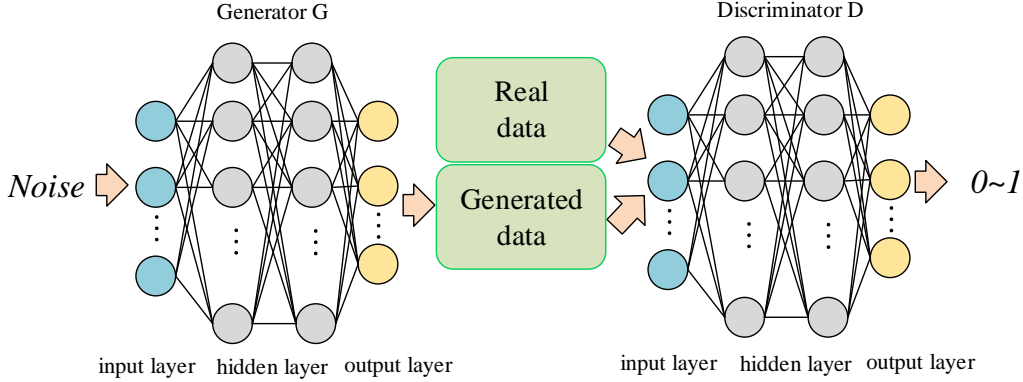


Fig. 2. The structure of a classic GAN.

large, or they are not stable. To overcome the drawbacks of existing models in flow field reconstructions and considering the characteristics of FFD, we prove that an RBFNN is the optimal discriminator of a GAN in next section. Based on this proof, the RBFNNs are introduced into GANs, which naturally form two novel GANs named RBF-GAN and the RBFC-GAN. Compared with existing approaches [50], [45], [51], these two models are more accurate and stable.

III. METHODOLOGY

A. Optimal Discriminator of GANs for Nonlinear Sparse Data generation

GoodFellow et al. proved that the optimal discriminator exists where $P_r(x) = P_g(x)$, i.e. $D(x) = 0.5$ [52]. However, the form of the optimal discriminator of a GAN was still unsolved. In this section, we first introduce the best approximation theory to clarify the nature of the neural networks to approximate given continuous functions, and then we prove that an RBFNN is the optimal discriminator while dealing with nonlinear sparse data come from these functions.

1) *The Best Approximation Problem:* The best approximation problem of neural networks could be stated as follows:

Definition III.1. Given a continuous function $F(X)$ belongs to function space Φ and a subset $A \subseteq \Phi$, find a function $f(W, X) \in A$ that depends continuously on $W \in R^n$ and X , such that

$$d(F(X), A) \equiv \inf_{f \in A} \|F(X) - f(W, X)\| \quad (3)$$

for all W in the set R^n , where $d(F(X), A)$ denotes the distance of $F(X)$ from subset A . If the infimum of $\|F(X) - f(W, X)\|$ is attained for some function $f(W^*, X)$ of A , we suppose that $f(W^*, X)$ is the best approximation for $F(X)$.

The approximation problem of neural networks is to construct a smooth mapping $f(W, X)$ between inputs and outputs from limited data. The smooth mapping denotes that small variations in inputs result in small variations in corresponding outputs. Paradoxically, the information contained in the nonlinear sparse datasets is not enough to reflect these small

variations. For example, unlike tens of thousands of samples in computer vision, the sample number of a general aerodynamic dataset is usually less than 1000 and hard to increase [6], [11], [41]. Besides, the high nonlinear characteristic of aerodynamic data undoubtedly increases the difficulty of approximations. Therefore, the best approximation is the only way to break this dilemma. Formula (3) denotes a function of the smooth mapping $f(W, X)$, whose minimum value can be calculated by Euler-Lagrange equation, which is introduced in next section.

It was proved that a FCN does not have the optimal approximation property for any continuous function, but an RBFNN does [53]. Therefore, in next sections, we prove a theorem that an RBFNN is the optimal discriminator of a GAN while dealing with nonlinear sparse data.

2) The Optimal Discriminator:

Theorem III.1. Assuming that $\mathcal{D} = \{(z_i, x_i) \in R^n | i = 1, \dots, N\}$ is a nonlinear and sparse dataset, where x_i denotes the real data, and z_i denotes the noise with a particular distribution, then the optimal discriminator of a GAN is an RBFNN.

Proof. To prove Theorem III.1, we introduce the regularization theory [53]:

$$\sum_i (f(x_i) - d_i)^2 + \lambda \|Pf(x)\|^2 \quad (4)$$

where $\sum_i (f(x_i) - d_i)^2$ is the original loss function of a neural network, which measures the distance between the generated data $f(x_i)$ and the real data d_i , $\|Pf(x)\|^2$ embeds a priori information on the function $f(x)$, P is a differential constrain operator [54], and λ is the coefficient of the regular term.

Based on (4), we write (1) as following:

$$L_D = -\mathbb{E}_{x \sim p_r(x)} [\log D(x)] - \mathbb{E}_{z \sim p_z(z)} [\log(1 - D(G(z)))] + \lambda \|PD(x)\|^2 \quad (5)$$

Formula (5) describes the loss function of $D(x)$, and can be written as the form of a functional:

$$H[D(x)] = -\mathbb{E}_{\mathbf{x} \sim p_r(\mathbf{x})}[\log D(\mathbf{x})] - \mathbb{E}_{\mathbf{z} \sim p_{\mathbf{z}}(\mathbf{z})}[\log(1 - D(G(\mathbf{z})))] + \lambda \|PD(x)\|^2 \quad (6)$$

As proved in [52], the loss function of a discriminator reached its minimum value while $D(x) = 0.5$, which means that the minimum value of (6) does exist. Therefore, the problem of the optimal discriminator of a GAN is to determine the function $D(x)$ such that (6) reaches its minimum value, which we use Euler-Lagrange equation to calculate the minimum value of $H[D(x)]$ to accomplish the optimal approximation defined in Theorem III.1.

Formula (6) could be expanded into a discrete form:

$$H[D(x)] = -\sum_{i=1}^N \{\mathbb{P}_r(x_i) \log D(x_i) + \mathbb{P}_g(x_i) \log[1 - D(x_i)]\} + \lambda \|PD(x)\|^2 \quad (7)$$

To minimize the functional $H[D(x)]$, we introduce the Euler-Lagrange equation [55]:

$$\frac{\partial L}{\partial f(x)} - \frac{d}{dx} \left(\frac{\partial L}{\partial f'(x)} \right) \equiv 0 \quad (8)$$

where L is a functional of x , $f(x)$ and $f'(x)$. Similarly, $H[\cdot]$ in (7) is a functional of x , $D(x)$ and $D'(x)$, i.e. $H[x, D(x), D'(x)]$. However, there is no $D'(x)$ in (7), the functional $H[\cdot]$ can be written as:

$$\begin{aligned} H[x, D(x), D'(x)] &= H(x, D(x)) \\ &= -\sum_{i=1}^N \{\mathbb{P}_r(x_i) \log D(x_i) + \mathbb{P}_g(x_i) \log[1 - D(x_i)]\} + \lambda \|PD(x)\|^2 \end{aligned} \quad (9)$$

From (9), we get:

$$\begin{cases} \frac{\partial H}{\partial D(x)} = -\sum_{i=1}^N [\mathbb{P}_r(x_i) \frac{1}{D(x_i)} - \mathbb{P}_g(x_i) \frac{1}{1-D(x_i)}] + 2\lambda \hat{P}PD(x) \\ \frac{d}{dx} \left(\frac{\partial H}{\partial D'(x)} \right) \equiv 0 \end{cases} \quad (10)$$

where \hat{P} is the adjoint of the differential constrained operator P .

Associated with (8) and (10), we get:

$$-\sum_{i=1}^N [\mathbb{P}_r(x_i) \frac{1}{D(x_i)} - \mathbb{P}_g(x_i) \frac{1}{1-D(x_i)}] + 2\lambda \hat{P}PD(x) = 0 \quad (11)$$

Then:

$$\hat{P}PD(x) = \frac{1}{2\lambda} \sum_{i=1}^N [\mathbb{P}_r(x_i) \frac{1}{D(x_i)} - \mathbb{P}_g(x_i) \frac{1}{1-D(x_i)}] \quad (12)$$

where, $\sum_{i=1}^N [\mathbb{P}_r(x_i) \frac{1}{D(x_i)} - \mathbb{P}_g(x_i) \frac{1}{1-D(x_i)}]$ in the right part represents the distance between the real data distribution and the generated data distribution, which is consistent with the training mechanism of GNAs, and $\hat{P}PD(x)$ represents the optimal discriminator constrained by the differential constrained operator P .

Since FFD in the training set is usually limited and sparse, it is hard to capture the small variations of inputs or outputs. Therefore, the information contained in every FFD should be fully utilized to achieve more accurate approximation than existing GANs. Based on (12), we introduce the Dirac function [56] that is widely used in the density problems in discrete distribution (or sparse data) in space or time to obtain :

$$\hat{P}PD(x) = \frac{1}{2\lambda} \sum_{i=1}^N [\mathbb{P}_r(x_i) \frac{1}{D(x_i)} - \mathbb{P}_g(x_i) \frac{1}{1-D(x_i)}] \delta(x-x_i) \quad (13)$$

where $\delta(x-x_i)$ is the Dirac function, implies that $D(x)$ is only activated where $x = x_i$ precisely and de-activated where $x \neq x_i$. To simplify (13), we introduce Green's function $R(x; y)$, which satisfies the following distributional formula [53]:

$$\hat{P}PR(x; y) = \delta(x - y) \quad (14)$$

The Dirac function $\delta(x - x_i)$ in (13) is replaced with (14) to get the following formula:

$$\begin{aligned} \hat{P}PD(x) &= \frac{1}{2\lambda} \sum_{i=1}^N [\mathbb{P}_r(x_i) \frac{1}{D(x_i)} \\ &\quad - \mathbb{P}_g(x_i) \frac{1}{1-D(x_i)}] \hat{P}PR(x; x_i) \end{aligned} \quad (15)$$

From (15), we derive the function $D(x)$:

$$D(x) = \frac{1}{2\lambda} \sum_{i=1}^N [\mathbb{P}_r(x_i) \frac{1}{D(x_i)} - \mathbb{P}_g(x_i) \frac{1}{1-D(x_i)}] R(x; x_i) \quad (16)$$

where $\mathbb{P}_r(x_i) \frac{1}{D(x_i)} - \mathbb{P}_g(x_i) \frac{1}{1-D(x_i)}$ is the distance of the real data from generated data. Let $w_i = \mathbb{P}_r(x_i) \frac{1}{D(x_i)} - \mathbb{P}_g(x_i) \frac{1}{1-D(x_i)}$ denotes the weights that the discriminator needs to learn, the function $D(x)$ can be written as in (17).

$$D(x) = \frac{1}{2\lambda} \sum_{i=1}^N w_i R(x; x_i) \quad (17)$$

In practical applications, the differential constrained operation P is rotationally and translationally invariant [54], therefore, R in (17) will depend on the difference of its arguments, i.e. $R(x; x_i) = R(\|x - x_i\|)$. Consequently, we get the final form:

$$D(x) = \frac{1}{2\lambda} \sum_{i=1}^N w_i R(\|x - x_i\|) \quad (18)$$

where the function $R(\cdot)$ could be replace with any radial basis function, for example Gaussian kernel function, and introduce the width σ , we get an RBFNN based on Gaussian kernel functions:

$$D(x) = \frac{1}{2\lambda} \sum_{i=1}^N w_i g_1(\mathbf{x}_i, \mathbf{v}, \sigma) \quad (19)$$

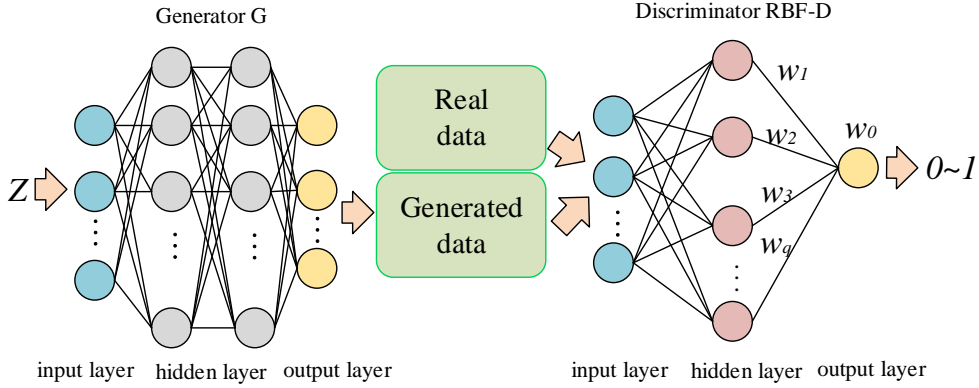


Fig. 3. The structure of an RBF-GAN. In the hidden layer of the discriminator D, the pink neurons represent RBFs. In this paper, we chose the Gaussian kernel function to realize the RBF-based discriminator D.

As a result, the loss function of a discriminator could be derived into a form of RBFNNs, which enables RBF-based discriminators to focus on the nonlinear and sparse data and ensure that the model has the minimum loss in the training set, that is, the hypersurface information contained in the training set is better utilized. Inspired by this theorem, RBFNNs can serve as the discriminator of a GAN while dealing with nonlinear sparse data. Therefore, we introduce the GANs based on RBFNNs (i.e. RBF-GAN and RBFC-GAN) in next subsection.

B. RBF-GAN and RBFC-GAN

1) *Overview*: We proposed an RBF-GAN and an RBFC-GAN based on the Theorem III.1 for nonlinear sparse data regression and generation. The RBF-GAN or RBFC-GAN also consists of a G and a D. The G is a FCN with multiple hidden layers. While the D is an RBFNN with only one hidden layers. We call the D in an RBF-GAN as the RBF-D, and similarly, the D in an RBFC-GAN is called the RBFC-D. In this section, we discuss the RBF-GAN and RBFC-GAN, separately.

2) *RBF-GAN*: We introduce multiple Gaussian kernel functions into (19) to form an novel RBF-D:

$$D(\mathbf{X}) = w_0 + \frac{1}{2\lambda} \sum_{i=1}^N \sum_{j=1}^q w_{ij} \cdot g_1(\mathbf{x}_i, \mathbf{v}_j, \sigma_j) \quad (20)$$

where \mathbf{X} denotes the input matrix, q denotes the number of Gaussian kernel functions, which equals to the number of hidden neurons in an RBF-D, N denotes the number of data \mathbf{X} , w_{ij} denotes the weight of the j th hidden neuron while dealing with the i th data, and w_0 denotes the bias of the only output neuron. We omit the coefficient $\frac{1}{2\lambda}$, and focus on a specific input vector \mathbf{x}_i , the (20) can be written as:

$$D(\mathbf{x}_i) = w_0 + \sum_{j=1}^q w_j \cdot g_1(\mathbf{x}_i, \mathbf{v}_j, \sigma_j) \quad (21)$$

where w_j denotes the weight between one hidden neuron and the only output neuron. This formula indicates that an RBF-based discriminator consists of three different layers: one input layer (i.e. \mathbf{x}_i), one hidden layer (i.e. the Gaussian kernel

function $\sum_{j=1}^q w_j g_1(\mathbf{x}_i, \mathbf{v}_j, \sigma_j)$) and one output layer (i.e. $D(\mathbf{x}_i)$). Fig.3 shows the structure of an RBF-GAN, where Z is a noise with a distribution \mathbb{P}_z , “Real data” denotes the data with distribution $\mathbb{P}_r(x)$, while “Generated data” with distribution $\mathbb{P}_g(x)$ denotes the data generated by G. The output of the RBF-D is a variable with a value between 0 and 1, which indicates the probability of the generated data is realistic.

3) *RBFC-GAN*: We replace the Gaussian kernel functions in (21) with multiple RBFs, then the following formula can be obtained:

$$D(\mathbf{x}_i) = \lambda_0 + \sum_{z=1}^m \lambda_z \sum_{j=1}^q w_{z,j} \cdot g_z(\mathbf{x}_i, \mathbf{v}_j, \sigma_j) \quad (22)$$

where m denotes the number of RBFs (i.e. the number of RBFNNs), q denotes the number of hidden neurons in every RBFNN, $w_{z,j}$ denotes the weight of the j th hidden neuron in the z th RBFNN, and λ_z denotes the coefficient for the z th RBFNN.

Formula (22) describes the structure of an RBFC-D that consists of one input layer (i.e. \mathbf{x}_i), one hidden layer (i.e. $\sum_{z=1}^m \lambda_z \sum_{j=1}^q w_{z,j} \cdot g_z(\mathbf{x}_i, \mathbf{v}_j, \sigma_j)$) and one output layer (i.e. $D(\mathbf{x}_i)$). Different from the RBF-D, the hidden layer of an RBFC-D consists of multiple clusters of RBFNNs. In this paper we call a RBFNN (i.e. $\sum_{j=1}^q w_{z,j} \cdot g_z(\mathbf{x}_i, \mathbf{v}_j, \sigma_j)$) as a cluster. Therefore, Fig.4 shows the structure conducted by (22) with $m = 3$, which means the RBFC-D consists of three different clusters (i.e. RBFNNs). The RBFs in every cluster are as follows:

$$\begin{cases} g_1(\mathbf{x}_i, \mathbf{v}_{j,1}, \sigma_{j,1}) = \exp\left(-\frac{\|\mathbf{x}_i - \mathbf{v}_{j,1}\|^2}{2\sigma_{j,1}^2}\right) \\ g_2(\mathbf{x}_i, \mathbf{v}_{j,2}, \sigma_{j,2}) = \exp\left(-\frac{\|\mathbf{x}_i - \mathbf{v}_{j,2}\|}{\sigma_{j,2}}\right) \\ g_3(\mathbf{x}_i, \mathbf{v}_{j,3}, \sigma_{j,3}) = \frac{1}{\sqrt{(\mathbf{x}_i - \mathbf{v}_{j,3})^2 + \sigma_{j,3}^2}} \end{cases} \quad (23)$$

where g_1 , g_2 and g_3 denotes the Gaussian kernel function, the Laplace kernel function and the inverse multiquadratics kernel function, respectively, $\mathbf{v}_{j,z}$ and $\sigma_{j,z}$ with $z = 1, 2, 3$ denote the center and width of j th RBF in z th RBFNN, respectively.

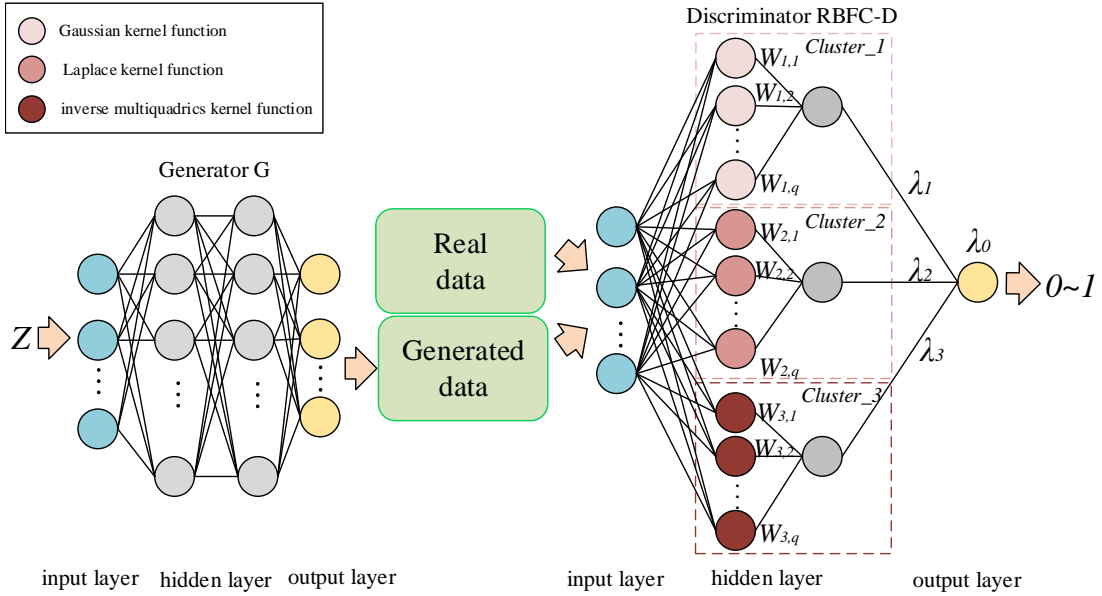


Fig. 4. The structure of an RBFC-GAN. Different from the RBF-D, the RBFC-D consists of multiple RBFNNs with different kernel functions. The RBFC-GAN is realized through combining different RBFNNs linearly.

IV. EXPERIMENTS AND RESULTS ANALYSIS

A. DataSets

To validate the effectiveness and feasibility of the RBF-GAN and the RBFC-GAN, three different datasets are employed, namely the Burgers' dataset, the cylindrical laminar dataset and the ONERA M6 dataset.

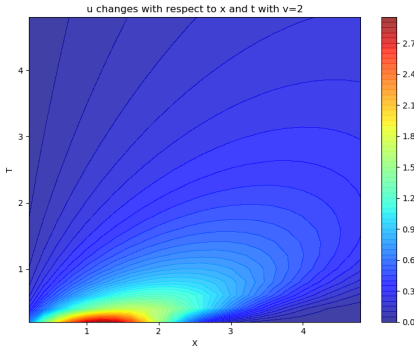


Fig. 5. The visualization results of the Burgers' Equation data. In this figure, the x-coordinate represents the displacement x , while the y-coordinate represents the time t .

1) Burgers' Dataset: The Burgers' equation is an one-dimensional PDE that expresses the movement of a shockwave across a tube:

$$\frac{\partial u}{\partial t} + u \frac{\partial u}{\partial x} = v \frac{\partial^2 u}{\partial x^2}$$

where u denotes the velocity of the fluid (the shockwave), t denotes the time, x denotes the displacement, and v denotes the viscosity coefficient. The variation range of design parameters (t , x and v) is from 0.2 to 4.8, and the step is 0.2. Consequently, this dataset contains 13824 samples. Fig.5 shows the variation of velocity u with respect to time t and

displacement x under the condition of $v = 2.0$. In this figure, the red part in the lower left corner describes the variations of high-velocity flows. Therefore, this Burgers' dataset contains limited high-velocity nonlinear data that can be used to verify whether the model will cause mode collapses.

2) Cylindrical Laminar Dataset: The cylindrical laminar dataset is a two-dimensional application of the Navier-Stokes equation that simulates the pressure change on the surface of a cylinder while a flow passes the cylinder. The Navier-Stokes equation is as follows:

$$\rho \left[\frac{\partial V}{\partial t} + (V \cdot \nabla) V \right] = -\nabla P + \rho g + v \nabla^2 V$$

where P , V , t , ρ , v denote the pressure, velocity, time, density and coefficient of viscosity, respectively. In this dataset, we used SU2 to calculate 6000 sample points [57]. The format and the variation range of the design parameters in this dataset are shown in Tab.I. The format of the response parameters is shown in Tab.II. Fig.6 shows the distribution of C_p around the cylindrical with $v = 2.0$.

variables	x	y	Ma
significance	x-coordinate	y-coordinate	mach number
start	0.1	-0.5	0.1
end	1	0.5	0.24
step	0.005	0.0078	0.01

TABLE I
THE DATA FORMAT AND VARIATION RANGE OF DESIGN PARAMETERS IN CYLINDRICAL LAMINAR DATASET.

3) ONERA M6 Dataset: The ONERA M6 dataset is given to describe the aerodynamic characteristics of a fixed ONERA M6 airfoil under different flow states [58]. We designed 770,000 grids (Fig.8) on the surface and the far field of the ONERA M6 airfoil to calculate 755 sample points using SU2. The format and the variation range of design parameters in this dataset are shown in Tab.III. The format of response

variables	P	C_p	F_x	F_y
significance	pressure	coefficient of pressure	the friction in the x-coordinate	the friction in the x-coordinate

TABLE II

THE DATA FORMAT OF RESPONSE PARAMETERS IN CYLINDRICAL LAMINAR TEST CASE.

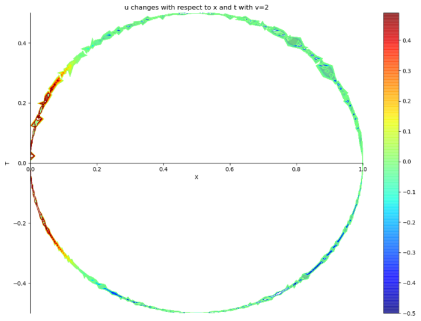


Fig. 6. The visualization results of the cylindrical laminar dataset. In this figure, the x-coordinate represents the displacement x , while the y-coordinate represents the time t .

parameters is shown in Tab.IV. We can see that the $AoA(\alpha)$ varies from 1.06 to 4.81, but there are only four different values, so the ONERA M6 dataset is a limited, non-linear and sparse dataset. Fig.7 illustrates the variation of coefficient of drag C_D , coefficient of pitching moment C_{M_y} , X component coefficient of friction C_{F_x} and coefficient of yawing moment C_{M_z} with $AoA(\alpha)$ when $Ma = 0.8$ and $Re = 8220000$.

variables	Ma	$AoA(\alpha)$	Re
significance	mach number	angle of attack	reynolds number
start	0.8045	1.06	8030000
end	0.8395	4.81	13000000
step	0.005	1.25	250000

TABLE III

THE DATA FORMAT AND VARIATION RANGE OF DESIGN PARAMETERS IN M6 TEST CASE.

B. Experimental Results

We compare 5 different neural networks, namely FCN [32], ClusterNet [11], GAN/cGAN [30], RBF-GAN and RBFC-GAN, among which the last three are generative models we pay special attention to. The learning rate is 0.0001, with the batch size 128, and the number of iterations 2000 within all models. The G of the generative models takes a 62 dimensional noise which follows a uniform distribution $U(0, 1)$ as a input. The initializations of centers and width of the hidden neurons in RBF-GAN or RBFC-GAN follow a uniform distribution $U(0, 1)$ and a normal distribution $N(0.5, 0.2)$, respectively. The five models compared in this paper are implemented based on tensorflow framework. All programs run on four Tesla K80 GPUs. The errors of these models are evaluated by MSE and MSPE:

$$\begin{cases} MSE = \frac{1}{n} \sum_{i=1}^n (f(x_i) - y_i)^2 \\ MSPE = \frac{1}{n} \sum_{i=1}^n \frac{\|f(x_i) - y_i\|^2}{\|y_i\|^2} \times 100\% \end{cases}$$

where y_i denotes the real response values, $f(x_i)$ denotes the generated response values under the same design parameters.

1) *Burgers' Dataset*: The Burgers' equation has numerical solutions, hence the model errors is evaluated using the Burgers' equation itself instead of validation sets or test sets. (i.e. there is no need to divide the whole datasets into training sets, validation sets and test sets). Tab.V shows the comparison results of the above models with the Burgers' dataset. We can learn that the RBF-GAN is more accurate than GAN, but worse than the FCN and the ClusterNet. Notably, the MSE and the MSPE of the RBFC-GAN are the lowest among these models.

To compare the ability of the three generative models to generate Burgers' data, the visualization results of velocity u generated by the GAN, the RBF-GAN and the RBFC-GAN in Tab.V are shown in Fig.9 and 10. From Fig.9, we can learn that the velocity u generated by GAN satisfies $u < 2.0$, which implies that the GAN can only generate low-velocity data, i.e. model collapse [59]. Compared with the GAN, the RBF-GAN can generate data with $u > 2.0$, which means that the RBF-GAN alleviates the problem of mode collapse. The RBFC-GAN is more accurate than the RBF-GAN, but still faces the problem of model collapse. Fig.10 also reflects the same results. The red part in the lower left corner of subgraph (c) is close to (a), which means that the RBF-GAN has the ability to generate high-velocity Burgers' data. Besides, compared with subgraph (b) and (c) in Fig.10, the contour lines in subgraph (d) show a smooth change, which is close to subgraph (a).

2) *Cylindrical Laminar dataset*: In the experiment of cylindrical laminar, we test the same neural networks as in Burgers' experiment. Unlike Burgers' dataset, the Navier-Stokes equation is more complex, and it is not realistic to calculate MSE and MSPE through this equation. Therefore, we divide the whole data set into three sets: a training set, a validation set and a test set with a ratio of 8:1:1. Considering the inability of GANs to generate data under specific flow states, we adopted cGANs to simplify the calculation of MSE and MSPE. Tab.VI shows the test errors of the five neural networks based on the cylindrical laminar dataset. We can learn that the RBF-cGAN and the RBFC-cGAN are more accurate than the cGAN, and similar with the FCN and the ClusterNet.

Fig.11 and 12 shows the pressure P and the friction in x-coordinate F_x generated by the cGAN, the RBF-cGAN and the RBFC-cGAN in Tab.VI, respectively. We can learn that the P and F_x generated by cGAN is less accurate than that of the RBF-cGAN and the RBFC-cGAN. Fig.13 shows the visualization results of coefficient of pressure C_p by CFD, the cGAN, the RBF-cGAN and the RBFC-cGAN. The four subgraphs in Fig.13 are similar, which indicates that the cGAN, the RBF-cGAN and the RBFC-cGAN can learn the distribution of pressure coefficient of cylindrical laminar dataset.

3) *ONERA M6 Dataset*: Similar with cylindrical laminar dataset, the whole ONERA M6 dataset are divided into a

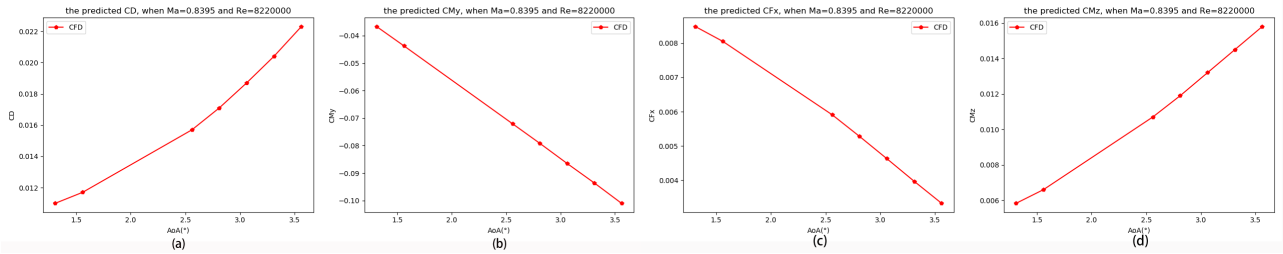


Fig. 7. The visualization results of coefficient of drag C_D (a), coefficient of pitching moment C_{M_y} (b), X component coefficient of friction C_{F_x} (c) and coefficient of yawing moment C_{M_z} (d) with $AoA(\alpha)$ under the condition of $Ma = 0.8$ and $Re = 8220000$.

variables significance	C_L coefficient of lift	C_D coefficient of drag	C_F coefficient of friction
variables significance	C_{M_x} coefficient of rolling moment	C_{M_y} coefficient of pitching moment	C_{M_z} coefficient of yawing moment
variables significance	C_{F_x} X component coefficient of friction	C_{F_y} Y component coefficient of friction	C_{F_z} Z component coefficient of friction

TABLE IV
THE DATA FORMAT OF RESPONSE PARAMETERS IN ONERA M6 DATASET.

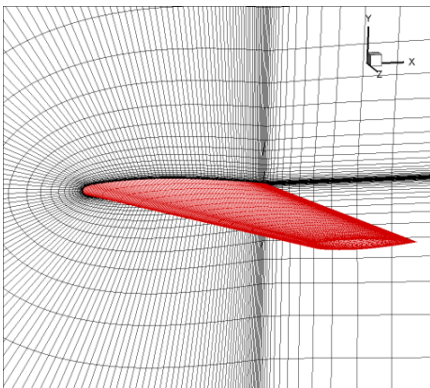


Fig. 8. The M6 wing and the grids on the surface and far field of the swing.

training set, a validation set and a test set with a ratio of 8:1:1. Besides, cGANs are still adopted in this dataset. In this experiment, the accuracy, stability and computational cost of the models are mainly discussed.

In terms of accuracy, we still choose MSE and MSPE as the indicators to evaluate the accuracy of models. Tab.VII shows the average errors of the ONERA M6 data generated by different models. We can learn that the RBF-cGAN and the RBFC-cGAN are more accurate than the cGAN, and similar to the FCN and the ClusterNet. Besides, the RBFC-cGAN is more accurate than the RBF-cGAN and the ClusterNet. Fig.14 and 15 show the C_D and C_{M_y} generated by three generative models. We can see that the C_D and C_{M_y} generated by the cGAN do not closely surround the 45-degree diagonal, but the data generated by the other two models are tightly clustered around the 45-degree diagonal. The visualization results of the remaining response parameters are similar. Fig.16 illustrates the variation of C_D , C_{M_y} , C_{F_x} and C_{M_z} with AoA respectively under the condition of $Ma = 0.8395$ and $Re = 8220000$. Compared with CFD, the data generated by cGAN always have large errors. As a result, the data generated by the RBF-cGAN and the RBFC-cGAN are more accurate

Method	Structure	MSE	MSPE
FCN	5,32	5.26×10^{-4}	5.92%
ClusterNet	4;1,1; 4,5	4.31×10^{-4}	5.36%
GAN	G(62,64*1,4) D(4,64*1,1)	2.07×10^{-3}	299.19%
RBF-GAN	G(62,1024*1,4) D(4,1024*1,1)	9.87×10^{-4}	10.86%
RBFC-GAN	G(62,128*2,4) D(4,(42,43,43),1)	8.21×10^{-5}	2.96%

TABLE V
THE TEST MSE AND MSPE OF THE FCN, THE CLUSTERNET, THE GAN, THE RBF-GAN AND THE RBFC-GAN BASED ON BURGERS' DATASET. IN THE COLUMN RELATED TO STRUCTURE, "5,32" MEANS THAT THE OPTIMAL FCN HAS 5 HIDDEN LAYERS, EACH HIDDEN LAYER HAS 32 NEURONS. "4;1,1; 4,5" MEANS THAT THE OPTIMAL CLUSTERNET CONSISTS OF 4 CLUSTERS, EACH OF WHICH CONSISTS OF A CONTEXT NETWORK AND A FUNCTIONAL NETWORK. THE CONTEXT NETWORK HAS 1 HIDDEN LAYER, EACH OF WHICH HAS ONLY ONE NEURON. THE FUNCTIONAL NETWORK HAS 4 HIDDEN LAYERS, EACH OF WHICH HAS 5 NODES. "G(62,128*2,4)" INDICATES THAT THE FCN-BASED GENERATOR HAS FOUR LAYERS, THE NUMBER OF NEURONS IN THE INPUT LAYER, AND THE OUTPUT LAYER IS 62 AND 4, RESPECTIVELY. "128*2" DENOTES THAT FCN-BASED GENERATOR HAS 2 HIDDEN LAYERS, EACH OF WHICH HAS 128 NEURONS. "D(4,(42,43,43),1)" INDICATES THAT THE RBFs CLUSTER-BASED DISCRIMINATOR HAS THREE LAYERS, 4 AND 1 DENOTES THE NUMBER OF NEURONS IN THE INPUT LAYER, AND THE OUTPUT LAYER, RESPECTIVELY. 42,43 AND 43 DENOTES THE NUMBER OF HIDDEN NEURONS OF THE GUASSIAN KERNEL-BASED RBFNN, THE LAPLACE KERNEL-BASED RBFNN AND THE INVERSE MULTIQUADRICS KERNEL-BASED RBFNN, RESPECTIVELY.

than that generated by the cGAN, and the RBFC-GAN is more accurate than RBF-cGAN.

In terms of stability, the validation errors (MSE) of the three generative models during the training process are compared in Fig.17. We can learn that when these three models converged (epoch > 750), the validation MSE of the RBF-cGAN and the RBFC-cGAN are lower than that of the cGAN, and the validation error of the RBFC-cGAN are lower than that of the RBF-cGAN. Besides, the RBF-cGAN converges faster than other models. According to the variation of the validation MSE of the three models, the entire iteration period is divided into three intervals, i.e. [0,125], [125,750] and [750,2000]. Tab.VIII illustrates the standard deviation of the validation MSE of the

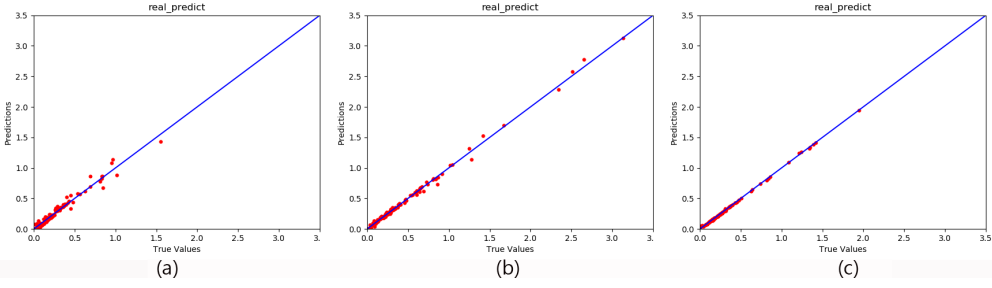


Fig. 9. The velocity u generated by GAN (a), RBF-GAN(b) and RBFC-GAN (c) in Burgers' dataset.

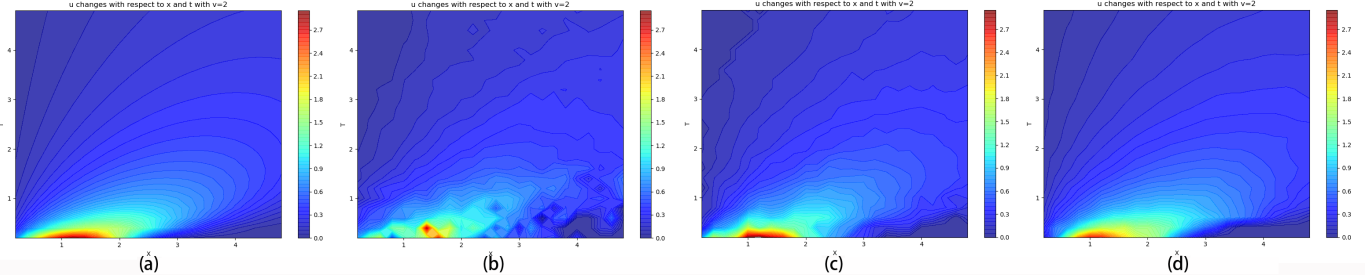


Fig. 10. The visualization results of velocity u generated by CFD (a), classic GAN (b), RBF-GAN (c) and RBFC-GAN(d).

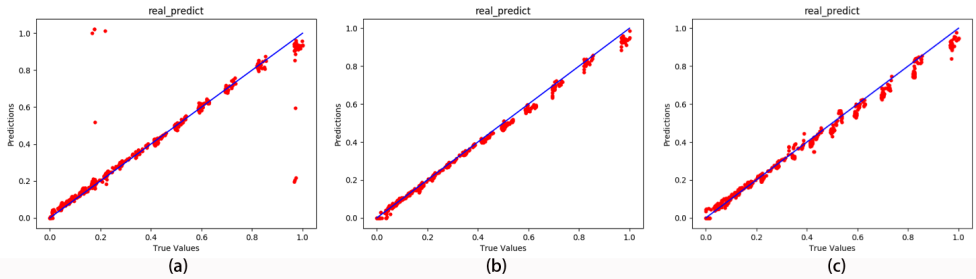


Fig. 11. The pressure P generated by cGAN (a), RBF-cGAN (b) and RBFC-cGAN (c).

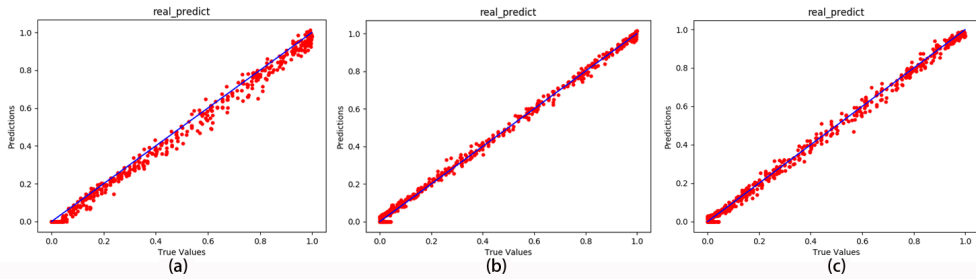


Fig. 12. The friction in the x-coordinate F_x generated data by cGAN (a), RBF-cGAN (b) and RBFC-cGAN (c).

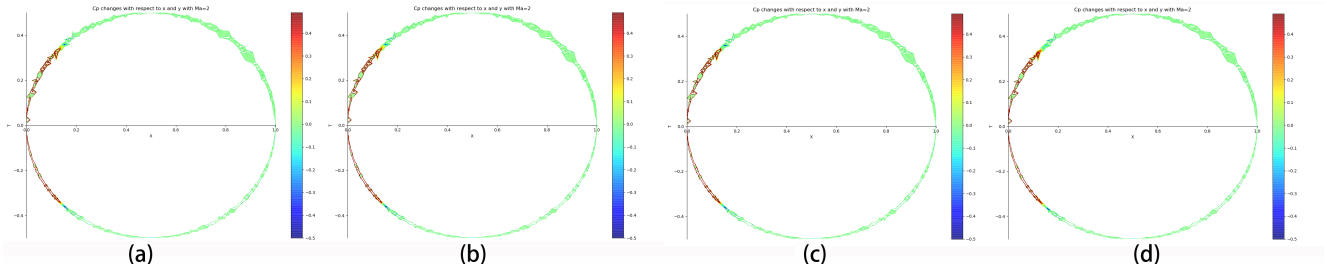
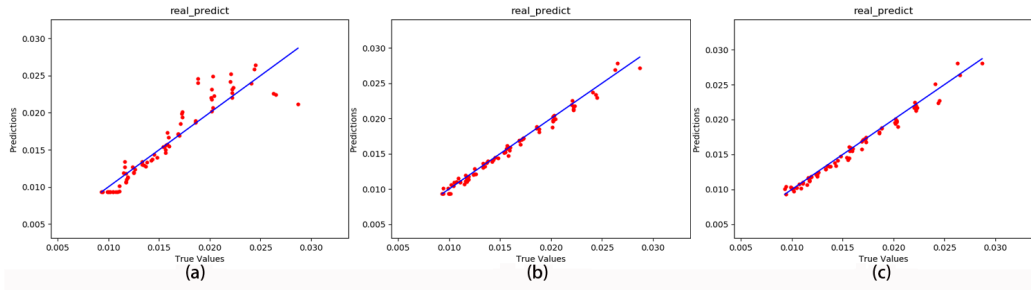
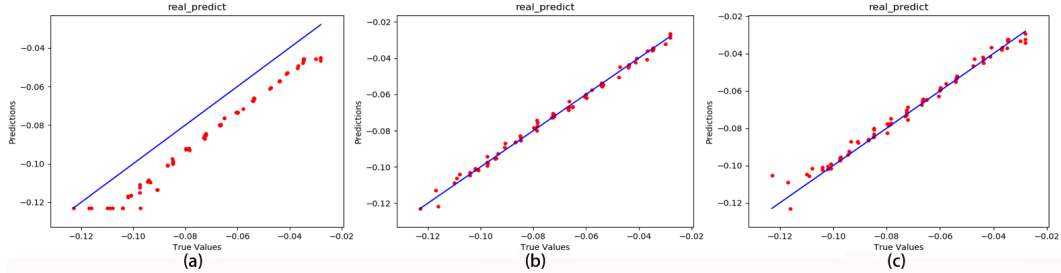
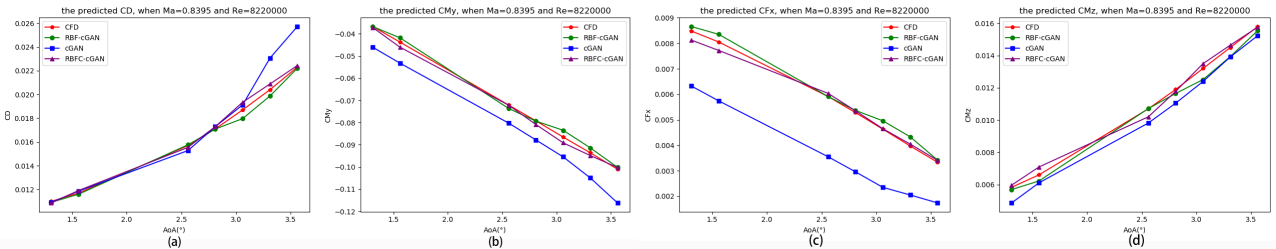


Fig. 13. The visualization results of coefficient of pressure C_p generated by CFD (a), classic GAN (b), RBF-GAN (c) and RBFC-GAN(d).

Fig. 14. The C_D generated by cGAN(a), RBF-cGAN(b) and RBFC-cGAN(c).Fig. 15. The C_{M_y} generated by cGAN(a), RBF-cGAN(b) and RBFC-cGAN(c).Fig. 16. The variation of drag coefficient C_D (a), coefficient of pitching moment C_{M_y} (b), X component coefficient of friction C_{F_x} (c) and coefficient of yawing moment C_{M_z} (d) with AoA under the condition of $Ma = 0.8395$ and $Re = 8220000$.

model	Structure	MSE	MSPE
FCN	5,64	2.48×10^{-4}	1.72%
ClusterNet	4;1,5,3,64	6.49×10^{-4}	4.73%
cGAN	G(62,512*1,4) D(7,512*1,1)	3.98×10^{-3}	6.40%
RBF-cGAN	G(62,512*2,4) D(7,512*1,1)	2.60×10^{-4}	2.05%
RBFC-cGAN	G(62,128*3,4) D(7,(42,43,43),1)	4.06×10^{-4}	4.42%

TABLE VI

THE TEST MSE AND MSPE OF THE FCN, CLUSTERNET, cGAN, RBF-cGAN AND RBFC-cGAN BASED ON CYLINDRICAL LAMINAR DATASET.

Method	Structure	MSE	MSPE
FCN	5 10	2.07×10^{-6}	0.23%
ClusterNet	4; 1 16; 3 32	8.29×10^{-6}	0.36%
cGAN	G(62,512,9) D(12,512,1)	5.48×10^{-5}	122.25%
RBF-cGAN	G(62,512,9) D(12,512,1)	1.90×10^{-5}	0.72%
RBFC-cGAN	G(62,128,9) D(12,(42,43,43),1)	1.24×10^{-5}	0.28%

TABLE VII

THE TEST MSE AND MSPE OF CLASSIC cGAN AND RBF-cGAN WITH M6 DATASET.

three models. The stability improvement η of a model after convergence is calculated using

$$\eta = \frac{||\hat{\sigma} - \sigma||}{||\sigma||} \times 100\%$$

where $\hat{\sigma}$ and σ denote standard deviations of two different models. Compared with cGAN, the stability improvement η_1 of RBF-cGAN and η_2 of RBFC-cGAN are 34.62% and

72.31%, respectively. However the stability improvement of RBFC-cGANs is based on the cost of convergence time.

As for the computational costs, because SU2 cannot run on GPU, we run all approaches on CPU to compare the average computational cost for generating a ONERA M6 data, which is shown in Tab.IX. In term of average time, SU2 takes the longest time to calculate a data, while the rest of models can output a data within 0.05 second, among which the FCN takes the shortest time to output a data, while the cGAN takes longest time to do so. Both of the RBF-cGAN and RBFC-

cGAN are faster than the cGAN, but slower than the FCN. In terms of hardware resources, SU2 occupies the most CPU and memory usage, followed by the clusterNet, the RBF-cGAN. The RBFC-cGAN, the cGAN and the FCN occupy the least hardware resources.

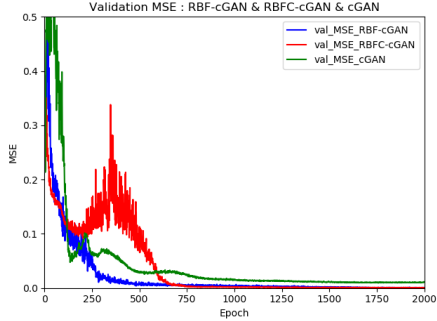


Fig. 17. The validation MSE during the training process of the three generative models.

models	[0,125)	[125,750)	[750,2000]	η
cGAN	0.16	0.027	0.0013	–
RBF-cGAN	0.082	0.048	0.00085	34.62%
RBFC-cGAN	0.082	0.074	0.00036	72.31%

TABLE VIII

THE STANDARD DEVIATION OF THE VALIDATION ERROR OF THE CGAN, RBF-cGAN AND RBFC-cGAN IN THREE INTERVALS DIVIDED ACCORDING TO THE TRAINING EPOCHS. η CALCULATED BY (24) DENOTES THE STABILITY IMPROVEMENT COMPARED WITH CGAN WHEN THE MODEL CONVERGES.

Method	Average time(s)	CPU usage(%)	Memory usage(MB)
SU2	6600	89	15194.33
FCN	0.0048	41.56	174.23
ClusterNet	0.0085	86.32	212.45
cGAN	0.024	53.00	176.82
RBF-cGAN	0.0206	76.21	186.98
RBFC-cGAN	0.0065	58.79	188.58

TABLE IX

THE AVERAGE COMPUTATIONAL COST OF APPROACHES TO OUTPUT A DATA WITH ONERA M6 DATASET.

C. Results Analysis

1) *The Errors:* Consider a simple Gaussian kernel function $K(x, v)$ with $\sigma = 1$:

$$\begin{aligned} K(x, v) &= \exp(-(x - v)^2) \\ &= \exp(-x^2) \cdot \exp(-v^2) \cdot \exp(2xv) \end{aligned} \quad (24)$$

where x and v denote the input and the center of $K(x, v)$, respectively. $\exp(2xv)$ can be expanded using the Taylor expansion:

$$\begin{aligned} K(x, v) &= \exp(-x^2) \cdot \exp(-v^2) \cdot \sum_{i=0}^{\infty} \frac{(2xv)^i}{i!} \\ &= \sum_{i=0}^{\infty} \exp(-x^2) \cdot \exp(-v^2) \sqrt{\frac{2^i}{i!}} x^i \sqrt{\frac{2^i}{i!}} v^i \end{aligned} \quad (25)$$

Let $\Phi(x) = \exp(-x^2) \cdot (1, \sqrt{\frac{2}{1}}x, \sqrt{\frac{2^2}{2!}}x^2, \dots)^T$, then $K(x, v) = \Phi(x) \cdot \Phi(v)$. As we can see, $\Phi(x)$ is an infinite dimensional vector, which demonstrated that the Gaussian kernel function maps low dimensional data into a higher dimensional space. The distance between two similar distributions in the low dimensional space (i.e. the input space) is magnified in a higher dimensional space (i.e. the hidden space). Hence, an RBF-D improves the ability to distinguish the real data from the generated data, which directly improves the quality of data generated by the corresponding generator.

In the RBFC-GAN, three different RBFs are linearly combined into a more complex multi-kernel RBF [8]. A multi-kernel RBF means that the low dimensional inputs can be mapped into a higher dimensional space than an RBF-GAN, which can further reduce the prediction error [11] under the condition of the same number of neurons.

2) *The Stability:* We still consider the $K(x, v)$ with $\sigma = 1$:

$$K(x, v) = \exp(-(x - v)^2) = \begin{cases} 1 & x = v \\ 0 & |x - v| \gg 0 \end{cases} \quad (26)$$

For any given input x , only hidden neurons whose center v closes to x are activated, which causes a small variation in $D(x)$. However, the hidden neurons of a FCN are all activated, which causes a relatively large variation in $D(x)$. Therefore, the RBF-GAN is more stable than FCN-based GANs.

Compared with the RBF-GAN, the form of clusters of RBFNNs can further improve the stability of the RBFC-GAN under the condition of the same number of neurons. In the RBFC-GAN, different RBFs are employed simultaneously to overcome the fluctuations of gradients. The gradients of weights in an RBFC-GAN are as follows:

$$\frac{\partial L_D}{\partial W_{zj}} = \frac{\partial L_D}{\partial D(x)} \cdot \frac{\partial D(x)}{\partial W_{zj}} = \frac{\partial L_D}{\partial D(x)} \cdot \lambda_z \cdot g_z(x_i, v_j, \sigma_j) \quad (27)$$

where L_D (5) denotes the loss function of the RBFC-D, W_{zj} denotes the weights of the RBFC-D. The gradient of weights in the RBFC-GAN does not fluctuates radically because the weighting of three different radial basis functions makes the value of $D(x)$ and L_D more stable after the RBFC-GAN converged.

3) *The computational cost:* In term of average time for generating a M6 data, the local updating strategy of RBFNNs accelerates the convergence procedure, which results in that both the RBF-GAN and RBFC-GAN are faster than the FCN-based GAN. Besides, the clusters of RBFC-GAN do not interfere with each other, and the scale of each cluster is relatively small, hence, the RBFC-GAN is faster than RBF-GAN. In term of hardware resources usages, the matrix multiplication in GANs is replaced by RBF, which is a more complex operator. Therefore, the hardware resources usage of RBF-GAN and RBFC-GAN are more than FCN and FCN-based GANs.

V. CONCLUSIONS

In this paper, the nonlinear full domain FFD generation and regression based on GANs is proposed. We firstly prove that an RBFNN is the optimal discriminator of a GAN while dealing

with nonlinear sparse data. Then, an RBF-GAN and an RBFC-GAN are further proposed. Compared with existing models, the RBF-GAN and the RBFC-GAN not only reduce the MSE and MSPE of generated FFD, but also improve the stability of GANs. Finally, three different datasets are used to validate the feasibility of our models. The detailed conclusions are as follows:

- a) we prove that an RBFNN is the optimal discriminator of a GAN while dealing with nonlinear sparse data;
- b) the RBF-GAN is more accurate and stable than GANs/cGANs in the field of flow field reconstructions;
- c) the RBFC-GAN is more accurate and stable than GANs/cGANs and RBF-GANs in the same field;
- d) compared with cGAN, the stability of RBF-cGAN and RBFC-cGAN improves by 34.62% and 72.31%, respectively.

In addition, we firmly believe that the proposed RBF-GAN and RBFC-GAN are not only suitable for flow field reconstructions, but also available for many other fields (e.g. the predictions of aerodynamic performance and optimization designs, etc) in the area of aerodynamics. Besides, the optimal generator of GANs is still unsolved, which will be one of our future works.

ACKNOWLEDGMENT

This work was supported by the National Numerical Wind Tunnel Project No.13RH19ZT6B1 and No.13RH19ZT62B.

Thanks to Professor. Zhonghua Han and Chenzhou Xu from School of Aeronautics, Northwestern Polytechnical University for providing us with technical support about SU2.

REFERENCES

- [1] J. Yu and J. S. Hesthaven, "Flowfield reconstruction method using artificial neural network," *Aiaa Journal*, vol. 57, no. 2, pp. 482–498, 2019.
- [2] J. Liu, W.-P. Song, Z.-H. Han, and Y. Zhang, "Efficient aerodynamic shape optimization of transonic wings using a parallel infilling strategy and surrogate models," *Structural and Multidisciplinary Optimization*, vol. 55, no. 3, pp. 925–943, 2017.
- [3] Y. Duan, Q. Zheng, and B. Jiang, "Use of computational fluid dynamics to implement an aerodynamic inverse design method based on exact riemann solution and moving wall boundary," *Engineering Applications of Computational Fluid Mechanics*, vol. 14, no. 1, pp. 284–298, 2020.
- [4] Z. Wang and J. Li, "3d simulation of flight control system for quad tilt rotor uav based on flightgear," *E&ES*, vol. 440, no. 5, p. 052056, 2020.
- [5] L. Sun and J.-X. Wang, "Physics-constrained bayesian neural network for fluid flow reconstruction with sparse and noisy data," *arXiv preprint arXiv:2001.05542*, 2020.
- [6] Y. Zhang, W. J. Sung, and D. N. Mavris, "Application of convolutional neural network to predict airfoil lift coefficient," in *2018 AIAA/ASCE/AHS/ASC Structures, Structural Dynamics, and Materials Conference*, 2018, p. 1903.
- [7] C. Lu, B. Jayaraman, J. Whitman, and G. Chowdhary, "Sparse convolution-based markov models for nonlinear fluid flows," *arXiv preprint arXiv:1803.08222*, 2018.
- [8] J. Kou and W. Zhang, "Multi-kernel neural networks for nonlinear unsteady aerodynamic reduced-order modeling," *Aerospace Science and Technology*, vol. 67, pp. 309–326, 2017.
- [9] V. Kumar, G. Singhal, V. K. Singh, and H. Srivastava, "Computational flow analysis of bubble formation dynamics in a liquid column subjected to high centrifugal force," in *IOP Conference Series: Materials Science and Engineering*, vol. 691, no. 1. IOP Publishing, 2019, p. 012049.
- [10] L. Hu, J. Zhang, Y. Xiang, and W. Wang, "Neural networks-based aerodynamic data modeling: A comprehensive review," *IEEE Access*, vol. 8, pp. 90 805–90 823, 2020.
- [11] C. White, D. Ushizima, and C. Farhat, "Fast neural network predictions from constrained aerodynamics datasets," in *AIAA Scitech 2020 Forum*, 2020, p. 0364.
- [12] D. Su, W. Zhang, and Z. Ye, "A reduced order model for uncoupled and coupled cascade flutter analysis," *Journal of Fluids and Structures*, vol. 61, pp. 410–430, 2016.
- [13] B. Glaz, L. Liu, and P. P. Friedmann, "Reduced-order nonlinear unsteady aerodynamic modeling using a surrogate-based recurrence framework," *AIAA journal*, vol. 48, no. 10, pp. 2418–2429, 2010.
- [14] A. Da Ronch, M. Ghoreyshi, and K. Badcock, "On the generation of flight dynamics aerodynamic tables by computational fluid dynamics," *Progress in Aerospace Sciences*, vol. 47, no. 8, pp. 597–620, 2011.
- [15] G. Chen, Y. Zuo, J. Sun, and Y. Li, "Support-vector-machine-based reduced-order model for limit cycle oscillation prediction of nonlinear aeroelastic system," *Mathematical problems in engineering*, vol. 2012, 2012.
- [16] A. Mannarino and P. Mantegazza, "Nonlinear aeroelastic reduced order modeling by recurrent neural networks," *Journal of Fluids and Structures*, vol. 48, pp. 103–121, 2014.
- [17] D. I. Ignat'ev and A. N. Khrabrov, "Neural network modeling of unsteady aerodynamic characteristics at high angles of attack," *Aerospace Science and Technology*, vol. 41, pp. 106–115, 2015.
- [18] J. Kou, W. Zhang, and M. Yin, "Novel wiener models with a time-delayed nonlinear block and their identification," *Nonlinear Dynamics*, vol. 85, no. 4, pp. 2389–2404, 2016.
- [19] H. Chen, L. He, W. Qian, and S. Wang, "Multiple aerodynamic coefficient prediction of airfoils using a convolutional neural network," *Symmetry*, vol. 12, no. 4, p. 544, 2020.
- [20] M. Milano and P. Koumoutsakos, "Neural network modeling for near wall turbulent flow," *Journal of Computational Physics*, vol. 182, no. 1, pp. 1–26, 2002.
- [21] D. Volkonskiy, I. Nazarov, and E. Burnaev, "Steganographic generative adversarial networks," in *Twelfth International Conference on Machine Vision (ICMV 2019)*, vol. 11433. International Society for Optics and Photonics, 2020, p. 11433M.
- [22] O. Tasar, S. Happy, Y. Tarabalka, and P. Alliez, "Colormpgan: Unsupervised domain adaptation for semantic segmentation using color mapping generative adversarial networks," *IEEE Transactions on Geoscience and Remote Sensing*, 2020.
- [23] W. Lira, J. Merz, D. Ritchie, D. Cohen-Or, and H. Zhang, "Ganhopper: Multi-hop gan for unsupervised image-to-image translation," *arXiv preprint arXiv:2002.10102*, 2020.
- [24] Y. Zhang, I. W. Tsang, Y. Luo, C.-H. Hu, X. Lu, and X. Yu, "Copy and paste gan: Face hallucination from shaded thumbnails," in *Proceedings of the IEEE/CVF Conference on Computer Vision and Pattern Recognition*, 2020, pp. 7355–7364.
- [25] L. Wu, Y. Xia, F. Tian, L. Zhao, T. Qin, J. Lai, and T.-Y. Liu, "Adversarial neural machine translation," in *Asian Conference on Machine Learning*, 2018, pp. 534–549.
- [26] B. Siddani, S. Balachandar, W. Moore, Y. Yang, and R. Fang, "Machine learning for physics-informed generation of dispersed multiphase flow using generative adversarial networks," *arXiv preprint arXiv:2005.05363*, 2020.
- [27] S. Lee and D. You, "Data-driven prediction of unsteady flow over a circular cylinder using deep learning," *Journal of Fluid Mechanics*, vol. 879, pp. 217–254, 2019.
- [28] J. Kim and C. Lee, "Deep unsupervised learning of turbulence for inflow generation at various reynolds numbers," *Journal of Computational Physics*, p. 109216, 2020.
- [29] Y. Xie, E. Franz, M. Chu, and N. Thuerey, "tempogan: A temporally coherent, volumetric gan for super-resolution fluid flow," *ACM Transactions on Graphics (TOG)*, vol. 37, no. 4, pp. 1–15, 2018.
- [30] A. B. Farimani, J. Gomes, and V. S. Pande, "Deep learning the physics of transport phenomena," *arXiv preprint arXiv:1709.02432*, 2017.
- [31] J. Moody and C. J. Darken, "Fast learning in networks of locally-tuned processing units," *Neural computation*, vol. 1, no. 2, pp. 281–294, 1989.
- [32] A. S. Tenney, M. N. Glauser, and J. Lewalle, "A deep learning approach to jet noise prediction," in *2018 AIAA Aerospace Sciences Meeting*, 2018, p. 1736.
- [33] H. H. Tan and K. H. Lim, "Vanishing gradient mitigation with deep learning neural network optimization," in *2019 7th International Conference on Smart Computing & Communications (ICSCC)*. IEEE, 2019, pp. 1–4.
- [34] M. Hočevá, B. Širok, and I. Grabec, "A turbulent-wake estimation using radial basis function neural networks," *Flow, turbulence and combustion*, vol. 74, no. 3, pp. 291–308, 2005.

- [35] K. Duraisamy, P. R. Spalart, and C. L. Rumsey, "Status, emerging ideas and future directions of turbulence modeling research in aeronautics," 2017.
- [36] M. Ghoreyshi, A. Jirásek, and R. M. Cummings, "Computational approximation of nonlinear unsteady aerodynamics using an aerodynamic model hierarchy," *Aerospace Science and Technology*, vol. 28, no. 1, pp. 133–144, 2013.
- [37] W. Zhang, L. Zhu, Y. Liu, and J. Kou, "Machine learning methods for turbulence modeling in subsonic flows over airfoils," *arXiv preprint arXiv:1806.05904*, 2018.
- [38] W. Zhang, B. Wang, and Z. Ye, "High efficient numerical method for limit cycle flutter analysis based on nonlinear aerodynamic reduced order model reduced order model," in *51st AIAA/ASME/ASCE/AHS/ASC Structures, Structural Dynamics, and Materials Conference 18th AIAA/ASME/AHS Adaptive Structures Conference 12th*, 2010, p. 2723.
- [39] L. Zhang, W. Zhou, and L. Jiao, "Wavelet support vector machine," *IEEE Transactions on Systems, Man, and Cybernetics, Part B (Cybernetics)*, vol. 34, no. 1, pp. 34–39, 2004.
- [40] G. Mordido, H. Yang, and C. Meinel, "microbatchgan: Stimulating diversity with multi-adversarial discrimination," *arXiv preprint arXiv:2001.03376*, 2020.
- [41] J. Li, M. Zhang, J. R. Martins, and C. Shu, "Efficient aerodynamic shape optimization with deep-learning-based geometric filtering," *AIAA Journal*, pp. 1–17, 2020.
- [42] M. Arjovsky and L. Bottou, "Towards principled methods for training generative adversarial networks. arxiv e-prints, art," *arXiv preprint arXiv:1701.04862*, 2017.
- [43] M. Arjovsky, S. Chintala, and L. Bottou, "Wasserstein gan," *arXiv preprint arXiv:1701.07875*, 2017.
- [44] A. Creswell, T. White, V. Dumoulin, K. Arulkumaran, B. Sengupta, and A. A. Bharath, "Generative adversarial networks: An overview," *IEEE Signal Processing Magazine*, vol. 35, no. 1, pp. 53–65, 2018.
- [45] J. Zhao, L. Xiong, P. K. Jayashree, J. Li, F. Zhao, Z. Wang, P. S. Pranata, P. S. Shen, S. Yan, and J. Feng, "Dual-agent gans for photorealistic and identity preserving profile face synthesis," in *Advances in neural information processing systems*, 2017, pp. 66–76.
- [46] J. Li, J. Jia, and D. Xu, "Unsupervised representation learning of image-based plant disease with deep convolutional generative adversarial networks," in *2018 37th Chinese Control Conference (CCC)*. IEEE, 2018, pp. 9159–9163.
- [47] H. Yang, D. Huang, Y. Wang, and A. K. Jain, "Learning face age progression: A pyramid architecture of gans," in *Proceedings of the IEEE Conference on Computer Vision and Pattern Recognition*, 2018, pp. 31–39.
- [48] H. Ye, L. Liang, G. Y. Li, and B.-H. Juang, "Deep learning based end-to-end wireless communication systems with conditional gan as unknown channel," *IEEE Transactions on Wireless Communications*, 2020.
- [49] X. Chen, Y. Duan, R. Houthooft, J. Schulman, I. Sutskever, and P. Abbeel, "Infogan: Interpretable representation learning by information maximizing generative adversarial nets," in *Advances in neural information processing systems*, 2016, pp. 2172–2180.
- [50] Y. Pan, M. Jin, S. Zhang, and Y. Deng, "Tec map completion using degan and poisson blending," *Space Weather*, vol. 18, no. 5, p. e2019SW002390, 2020.
- [51] K. Wang and X. Wan, "Sentigan: Generating sentimental texts via mixture adversarial networks," in *IJCAI*, 2018, pp. 4446–4452.
- [52] I. Goodfellow, J. Pouget-Abadie, M. Mirza, B. Xu, D. Warde-Farley, S. Ozair, A. Courville, and Y. Bengio, "Generative adversarial nets," in *Advances in neural information processing systems*, 2014, pp. 2672–2680.
- [53] F. Girosi and T. Poggio, "Networks and the best approximation property," *Biological cybernetics*, vol. 63, no. 3, pp. 169–176, 1990.
- [54] T. Poggio and F. Girosi, "Networks for approximation and learning," *Proceedings of the IEEE*, vol. 78, no. 9, pp. 1481–1497, 1990.
- [55] R. Courant and D. Hilbert, "1962 methods of mathematical physics, vol. 2," *New York: Interscience*, p. 35.
- [56] V. A. Yerokhin and A. V. Maiorova, "Calculations of qed effects with the dirac green function," *Symmetry*, vol. 12, no. 5, p. 800, 2020.
- [57] S. Vitale, M. Pini, and P. Colonna, "Multistage turbomachinery design using the discrete adjoint method within the open-source software su2," *Journal of Propulsion and Power*, vol. 36, no. 3, pp. 465–478, 2020.
- [58] A. Balan, M. A. Park, W. K. Anderson, D. S. Kamenetskiy, J. A. Krakos, T. Michal, and F. Alauzet, "Verification of anisotropic mesh adaptation for turbulent simulations over onera m6 wing," *AIAA Journal*, vol. 58, no. 4, pp. 1550–1565, 2020.
- [59] D. Bang and H. Shim, "Mggan: Solving mode collapse using manifold guided training," *arXiv preprint arXiv:1804.04391*, 2018.



Liwei Hu received his B.S. degree in software engineering from the School of Software, Hebei Normal University, Shijiazhuang, Hebei, China, in 2014 as well as an M.S. degree in computer technology from the University of Electronic Science and Technology of China (UESTC), Chengdu, Sichuan, China, in 2018. He is currently pursuing a Ph.D. degree in computer science and technology from the School of Computer Science and Engineering, UESTC. His research fields include aerodynamic data modeling, deep learning and pattern recognition.



Wenyong Wang received his B.S. degree in computer science from BeiHang University, Beijing, China, in 1988 and M.S. and Ph.D. degrees from the University of Electronic Science and Technology (UESTC), Chengdu, China, in 1991 and 2011, respectively. He has been a professor in computer science and engineering at UESTC since 2006. Now he is also a special-term professor at Macau University of Science and Technology, a senior member of the Chinese Computer Federation, a member of the expert board of the China Education and Research Network (CERNET) and China Next Generation Internet. His main research interests include next generation Internet, software-defined networks, and software engineering.



Yu Xiang received his B.S., M.S. and Ph.D. degrees from the University of Electronic Science and Technology of China (UESTC), Chengdu, Sichuan, China, in 1995, 1998 and 2003, respectively. He joined the UESTC in 2003 and became associate professor in 2006. From 2014–2015, he was a visiting scholar at the University of Melbourne, Australia. His current research interests include computer networks, intelligent transportation systems and deep learning.



Jun Zhang received his B.S. and M.S. degrees in electronic engineering from the University of Electronic Science and Technology of China (UESTC) in 1995 and 1998, respectively. From 1998 to 2008, he worked as a senior researcher and engineer in CERNET. He is currently a lecturer at the School of Computer Science and Engineering, UESTC. His current research interests include software-defined networks, machine learning applied in network traffic engineering, and aerodynamics.